

Synthesis of Ag-loaded Sb₂WO₆ microsphere with enhanced photocatalytic ability for organic dyes degradations under different light irradiations

Shunqiang Chen ^a, Maoyuan Zhou ^a, Taohai Li^{*a}, and Wei Cao^b

^a*College of Chemistry, Key Lab of Environment Friendly Chemistry and Application in Ministry of Education, Xiangtan University, Xiangtan, 411105, China.*

^b*Nano and Molecular Systems Research Unit, Faculty of Science, University of Oulu, P.O. Box 3000, FIN-90014, Finland.*

* Correspondence Author. Tel.: +86-731-58292202; fax: +86-731-8292251;
E-mail address: hnlth@xtu.edu.cn(T. Li)

Abstract

In this study, the Ag-loaded Sb_2WO_6 photocatalysts have been successfully synthesized by a facile solvothermal method. The as-prepared Ag doping Sb_2WO_6 microspheres were characterized by X-ray diffraction (XRD), scanning electron microscope (SEM), high-resolution transmission electron microscopy (HRTEM), high angle annular dark-field transmission electron microscopy (HAADF-STEM), energy-dispersive X-ray spectroscopy (EDS), X-ray photoelectron spectroscopy (XPS), UV-Vis diffuse reflectance spectroscopy (UV-DRS) and the Brunauer–Emmett–Teller (BET) method. Results indicate that metallic Ag was successfully grown on Sb_2WO_6 . The photocatalytic activities of the Ag- Sb_2WO_6 photocatalysts were evaluated by degradations of MO, RhB and MB under UV light and visible light. It is found that the photocatalytic activity is excellent and superior after the decoration of the metallic Ag nanoparticles. A possible photocatalytic mechanism was proposed.

Keywords: Ag doping Sb_2WO_6 ; Solvothermal; Microspheres; Photocatalytic

1. Introduction

Pollution becomes a serious and worldwide problem following the accelerations of industrialization and urbanization. Environmentally harmful wastewater is one of the most common polluted substances within such an issue [1, 2]. In most cases, wastewater often contains high-level organic pollutants such as phenol and polychlorinated biphenyls. It causes considerable damages to ecosystem and human health due to high toxicities and carcinogenic characters of the pollutants [3-5]. Up to date, various methods have been developed to decontaminate pollutants in wastewater. Among them, photocatalysis is considered as the most promising cleantech thanks to its efficient, economical, and environmentally viable merits [6-9].

As a heterogeneous semiconductor photocatalyst, the Aurivillius-structured bismuth tungstate (Bi_2WO_6) has attracted enormous attentions due to its excellent materials properties such as non-toxicity, resistance to corrosion, and ferroelectric features [10-15]. Similar to the Bi_2WO_6 , the Sb_2WO_6 consists of perovskite ($\text{A}_{m-1}\text{B}_m\text{O}_{3m+1}$) layers that are composed with the $(\text{WO}_4)_2$ and $(\text{Sb}_2\text{O}_2)^{2+}$. As a typical n-type semiconductor, it can also be employed as an efficient photocatalyst [16-18]. However, the synthesis of the Sb_2WO_6 was scarcely reported [16]. Furthermore, its catalytic ability is still limited due to high recombination rate of photo-generated electron-hole pairs in the process of photocatalytic reaction. This common problem in photocatalysis may be solved via materials engineering routes such as shape tuning, combination with noble metal elements. It is noticed that metal nanoparticle loading can hold the photoexcited electrons and induce plasmonic effect [17 Cao, Mat. Phys.

Chem. 158: 89-95 (2015)], resulting in improvement of the separation efficiency of photo-generated charges. Especially, the catalytic activity is substantially enhanced when noble metals, such as Au, Ag, Cu and Pt nanoparticles are introduced into the semiconductors [19-21]. Thus it is interesting to investigate the photocatalytic activity of noble metal doped Sb_2WO_6 .

In the present study, the Ag-loaded Sb_2WO_6 microspherical photocatalysts have been successfully synthesized by a facile hydrothermal method. The as-prepared Ag- Sb_2WO_6 photocatalysts showed higher photocatalytic abilities than the corresponding pure Sb_2WO_6 in degradations of Methyl orange (MO), Rhodamine B (RhB) and Methylene blue (MB) aqueous solution under UV light and visible light irradiation. Moreover, a possible photocatalytic mechanism of photoelectron-hole pairs separation and transfer was proposed.

2. Experimental

2.1. Preparation of Ag- Sb_2WO_6 microspheres

Sodium tungstate ($\text{Na}_2\text{WO}_4 \cdot 2\text{H}_2\text{O}$, analytical grade), antimony trichloride (SbCl_3 , analytical grade) and silver nitrate (AgNO_3 , analytical grade) were employed as tungsten, antimony and silver sources. All the other chemicals used in the experiments were also of analytic reagent grade without further purification. Deionized water was used throughout the experiment.

The catalysts were synthesized by a facile hydrothermal method. The preparation was carried as follows: 1 mmol sodium tungstate ($\text{Na}_2\text{WO}_4 \cdot 2\text{H}_2\text{O}$) was suspended in 8 mL deionized water at room temperature under stirring until it dissolved completely.

2 mmol antimony trichloride (SbCl_3) was dissolved in 8 mL absolute ethanol to form a solution. Then the antimony trichloride solution was dripped into the sodium tungstate aqueous. The resulting yellowish suspension was stirred for 10 min. Then 0.2 mmol (0.4 mmol, 0.6 mmol) silver nitrate (AgNO_3) was added into the suspension. Here the $[\text{AgNO}_3]: [\text{SbCl}_3]$ molar ratio was tuned to 10% (20%, 30%). Under vigorous stirring for 30 min, the pH value of the suspension was adjusted to 2 by the dripping of 1 mol/L NaOH/HNO_3 solution. After being stirred 10 min, the suspension was transferred into a 20 mL Teflon-lined stainless steel autoclave. Then the autoclave was sealed, heated under autogenous pressure at 180°C for 24 h, and then cooled down to room temperature. The obtained product was filtrated and washed three times with absolute ethanol and deionized water, finally dried at 60°C in vacuum for 12 h. Samples were named S1 ($[\text{AgNO}_3]: [\text{SbCl}_3] = 10\%$), S2 ($[\text{AgNO}_3]: [\text{SbCl}_3] = 20\%$) and S3 ($[\text{AgNO}_3]: [\text{SbCl}_3] = 30\%$) in turn. For comparison purposes, the Sb_2WO_6 without Ag loading was prepared by the same above mentioned method and labeled as S0.

2.2. Characterizations of Ag- Sb_2WO_6 microspheres

The crystal structure of the synthesized catalysts were characterized by X-ray diffraction (XRD) on a Rigaku D/max-2500 diffractometer at 40 kV and 40 mA with $\text{Cu-K}\alpha$ radiation in a 2θ range of 10° to 90° . The morphology of the photocatalysts was observed using a JEOL JSM-6700F scanning electron microscope (SEM). TEM images, HRTEM images, HAADF-STEM images and EDS elemental mapping images of the catalysts were obtained by high-resolution transmission electron microscopy (JEM 2014) at 200 kV. X-ray photoelectron spectroscopy (XPS)

measurements were recorded on a PHI5300 with a monochromatic Mg K α X-ray as the excitation source to explore the elements and chemical states on the surface. Binding energy was calibrated with respect to the signal for C 1s of 284.8 eV. The UV-Vis diffuse reflectance spectrum was measured using a UV-2550 Shimadzu ultraviolet visible near infrared spectrophotometer in the range of 200–800 nm. Nitrogen adsorption–desorption isotherms were carried out on a nitrogen adsorption apparatus (TRISTAR II 3020, USA).

2.3. Photodegradation experiments

The photocatalytic activities of the as-prepared samples (50 mg) for RhB, MB and MO degradation were tested by measuring the concentration of RhB, MO and MB (50mL) in aqueous solutions. Initial concentrations of dyes were 10 mg/L. The degradation reaction was conducted under irradiations of ultraviolet light (using an Hg lamp equipped with a 365 nm cut-off filter, 500 W), visible light (using a 300 W xenon lamp with a 420 nm cut-off glass filter) for 3 h (or 2 h). The dye solution was placed into a cylindrical glass reactor (diameter 12.5 cm; height 6 cm). The distance between the sample and lamp was 10 cm. During the reaction, a water-cooling system cooled the water-jacketed photochemical reactor was used to maintain the dye solution at about 25°C. To eliminate the adsorption/desorption equilibrium effects of RhB, MO and MB on the samples, all the sample dye mixtures were stirred magnetically in the dark for 30 min before the UV irradiation. Each 30 minutes (or 20 min), 4 mL solution was taken out and centrifuged to remove the catalysts. The colour of the samples was detected by a lambda 25 UV-Vis spectrophotometer (Perkin-Elmer,

USA) with a scan range of 300-700 nm. The quartz colorimetric cell was used for recording the absorption spectra at ambient temperature. The RhB, MO and MB absorption peaks locate at 552, 462 and 664 nm, respectively. They were used to detect the degradation of RhB, MO and MB. The final degraded solution samples for MB under visible light were tested by TOC (total organic carbon) analysis on a Shimadzu TOC L-CPH analysis meter.

3. Results and discussion

3.1. Structural analysis

Fig. 1 shows the powder XRD patterns of the as-prepared samples. For comparison purpose, those of metallic Ag and Sb_2WO_6 (JCPDS) were also provided. It can be seen that all the diffraction peaks of the as-prepared sample without Ag are readily in accordance with 2θ values of Sb_2WO_6 (JCPDS NO.47-1680). Diffraction peaks at $2\theta=20.3^\circ$, 26.8° , 29.2° , 29.89° , 40.2° , 47.31° and 48.57° are indexed to the (011), (111), (003), (11-2), (202), (02-3) and (114) crystal planes, respectively. No characteristic diffraction peaks of other impurity phases were detected. And the peaks of Sb_2WO_6 were also observed in other samples. The diffraction peaks at 38.12° , 44.27° , 64.43° can be assigned to the (111), (200), (220) reflections of the metallic Ag (JCPDS NO.04-0783), respectively. After introducing the Ag to the composites, the (111) plane at $2\theta=26.8^\circ$ of Sb_2WO_6 has an obvious redshift, denoting a distortion of Sb_2WO_6 crystal lattice. Meanwhile, XRD peaks of the metallic Ag become more pronounced following the Ag content increase. No shift was observed for these peaks. Thus, change of Sb_2WO_6 lattice and emerging of Ag peaks prove the successful

combination of the metallic Ag with the semiconductivtve Sb_2WO_6 .

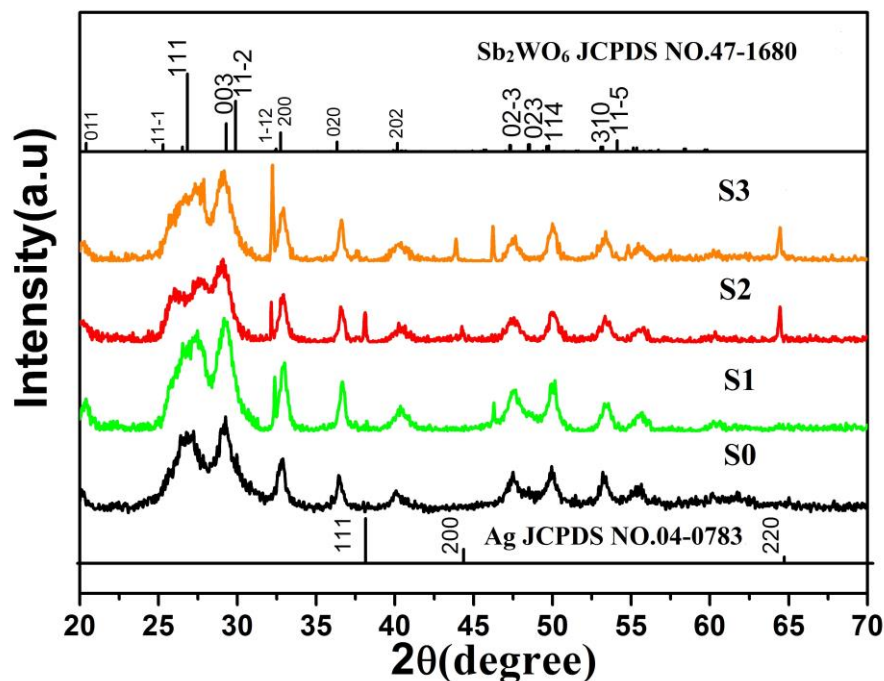


Fig. 1

3.2. Morphology analysis

The SEM images of the as-prepared samples are given in Fig. 2. From Fig. 2a, it is clear that the pure Sb_2WO_6 sample has obvious layered microsphere structures piled up from a large quantities of smooth microsheets and microwires with length about $1\mu\text{m}$. S1 and S2 also show a microspherical morphology, but the nanosheets and nanowires become shorter and thinner compared to S0. This is due to the existence of element Ag significantly tunes the morphology of the Sb_2WO_6 matrix. Moreover, more decorating Ag nanoparticles lead to rougher Sb_2WO_6 surface. At the 30% Ag load, the nanowires and nanosheets turn to slenders and stretch out from the

microspheres (Fig. 2d).

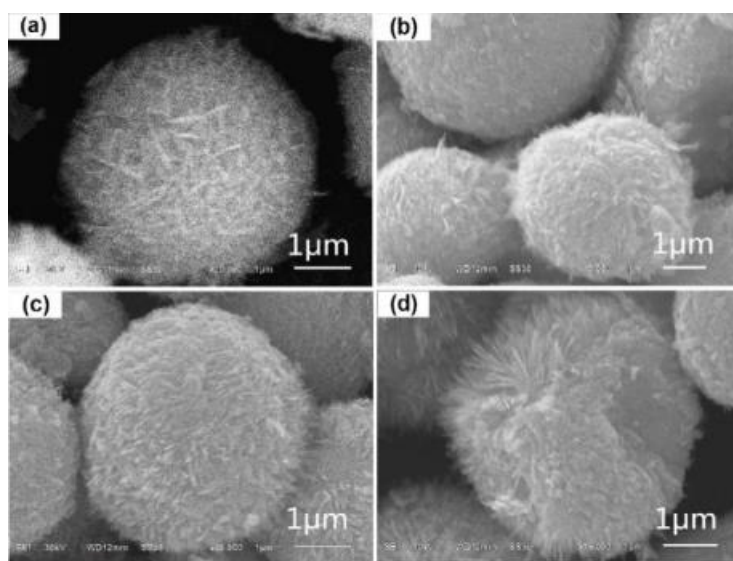


Fig. 2

In order to confirm the results obtained from XRD and SEM, we carried out TEM and HRTEM to explicate the structure of the as-prepared photocatalysts. From the TEM images of Fig. 3a-c, it is obvious that the samples own a well-defined microspherical shape. The diameter of the microspheres are within 5.0-5.8 μm , with an average value of $\sim 5.5 \mu\text{m}$. The microspheres are piled up from a large number of nanosheets with a width of about 15-25 nm. The results are consistent with the SEM observation. Images taken from the edge of the individual microsphere are used to further investigate the composition of the sample. As shown in Fig. 3c, materials are highly crystallized. Fig. 3c also shows many Ag nanoparticles with an average diameter of 6-10 nm were loaded in the nanosheets. In addition, from the HRTEM image shown in Fig. 3d, the lattice fringe of $d=0.236 \text{ nm}$ matches well to the (111) plane of the Ag nanoparticles, and the lattice fringes with an interplanar spacing of

0.206 nm, 0.217 nm, 0.224 nm and 0.221 nm can be attributed to the (122), (121), (202) and (121) facets of Sb_2WO_6 , respectively. The nanoparticles were also found in the interior of nanosheets, further indicating that the successful loading of the Ag nanoparticles in the Sb_2WO_6 photocatalysts.

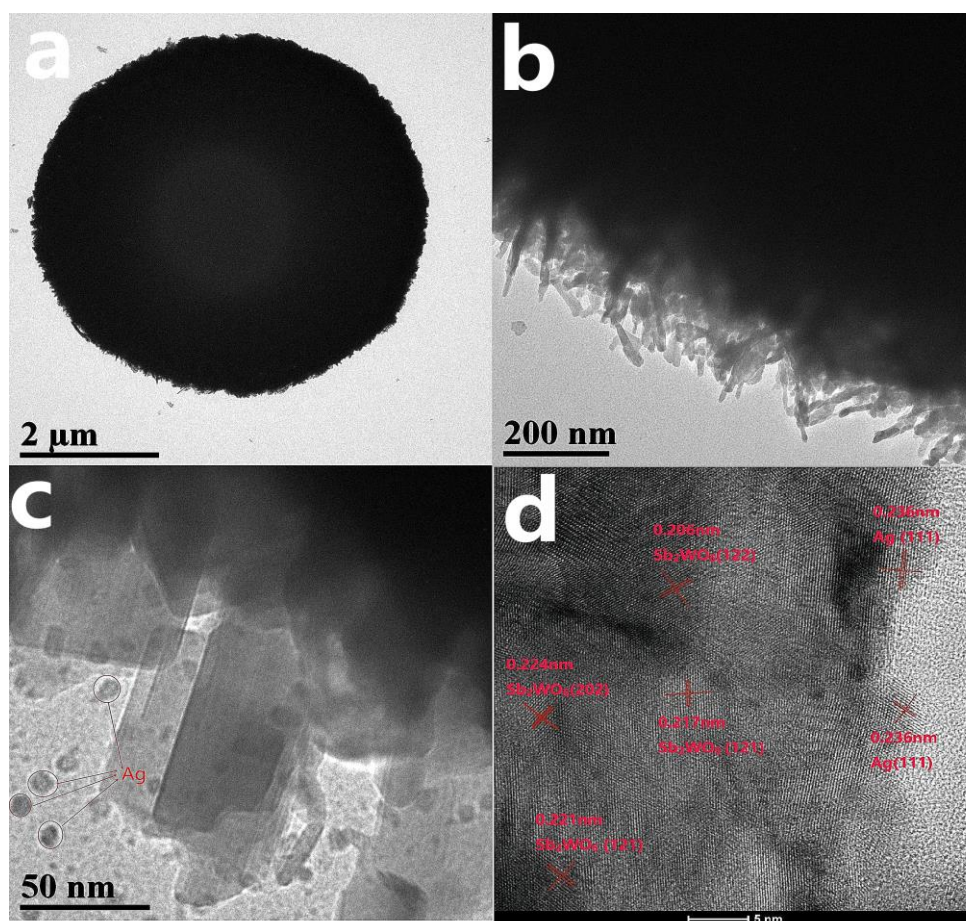


Fig. 3

To study more structural information about the Ag- Sb_2WO_6 composites, the high angle annular dark-field transmission electron microscopy (HAADF-STEM) and EDS elemental mapping images of S2 were used to further confirm the distribution of Ag NPs, which are shown in Fig. 4a-g, confirming the existence of Ag, O, Sb and W

elements in the Ag-loaded Sb_2WO_6 . As shown in Fig. 4a and b, some bright spots on the Ag- Sb_2WO_6 microsphere surface should be ascribed to Ag nanoparticles, and the Ag deposited on the surface of Sb_2WO_6 layered microsphere can also be confirmed by the signal intensity of different elements. The STEM images and EDS mappings confirm that Ag is highly dispersed on the Sb_2WO_6 layered microsphere substrate.

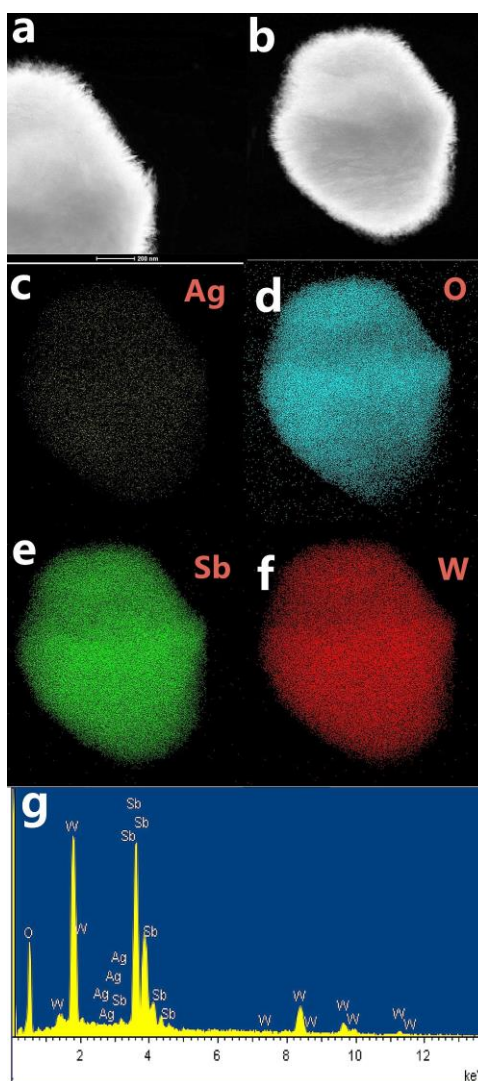


Fig. 4

3.2. XPS analysis

XPS analyse was performed to elucidate the chemical states of constituent elements and the chemical compositions on the surface for as-prepared samples. Fig. 5f shows a full survey of S2, where Sb, W, Ag, and O are detected in the photocatalysts. The peak at 284.78 eV (Fig. 5d) is assigned to adventitious carbon 1s, and it was used for reference [22]. The high resolution XPS spectrum of the Sb 3d was obtained to gain insight into the Sb state, as given in Fig. 5a. Two peaks at 539.8 eV and 530.4 eV are corresponding to 3d_{3/2} and 3d_{5/2} of the Sb³⁺, respectively [23, 24]. Peaks at 37.7 and 35.6 eV, respectively belong to 4f_{5/2} and 4f_{7/2} (Fig. 5c) of the W⁶⁺ oxidation state [25]. Moreover, the characteristic signal of O 1s in the S2 photocatalysts locates at 530.38 eV. The rather broad nature may arise from O of two chemical states: crystal lattice oxygen and surface adsorbed oxygen [26]. The peaks at 372.58 and 366.68 eV can be respectively assigned to 3d_{3/2} and 3d_{5/2} of the metallic Ag. These peaks bear small redshifts in the samples, which can be ascribed to the possible interaction between the Ag and Ag⁺, due to small amount of Ag⁺ existed in samples [34]. The XPS data confirms the existence of metallic Ag in Sb₂WO₆.

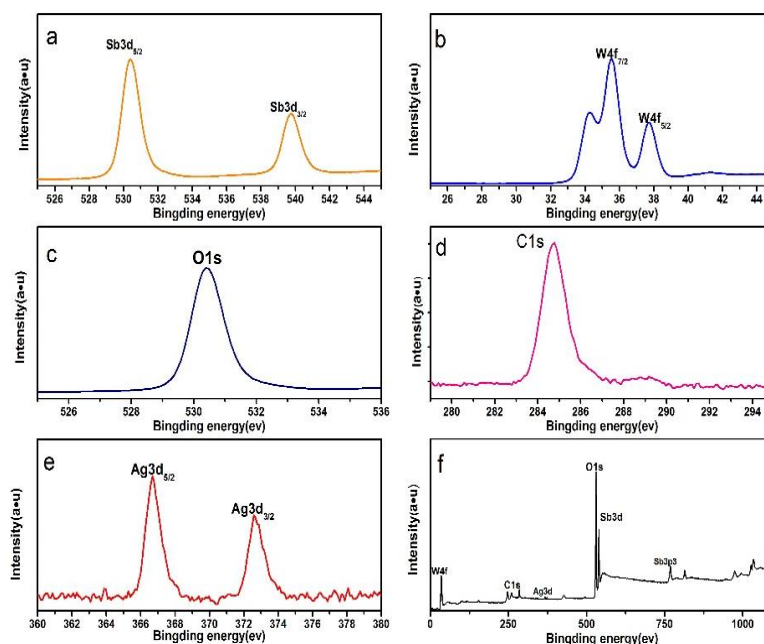


Fig. 5

3.3 Optical properties

The optical properties of the as-synthesized samples are shown in Fig. 6. It is obvious that the adsorption edge of pure Sb_2WO_6 (S0) centred at about 500 nm, exhibiting weak adsorption in the visible light regions. Then, the as-prepared Ag doped Sb_2WO_6 samples (S1, S2 and S3) have strong adsorption in the visible regions with adsorption edge between 500 and 550 nm. The band gap energy E_g of the as-prepared samples can be calculated by the formula: $E_g = 1240/\lambda$, where λ is the band gap wavelength. Band gaps are calculated to be 2.46, 2.30, 2.33 and 2.29 eV for S0, S1, S2 and S3, respectively. From the Fig. 6, it can conclude that all the samples exhibit photo-adsorption abilities in the visible light regions. Such an optic property refers to possible usages as photocatalyst under visible light irradiation.

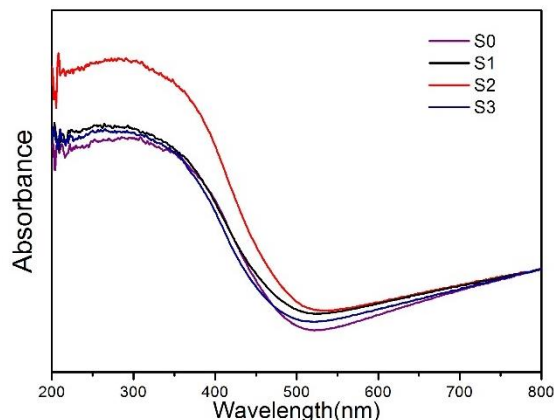


Fig. 6

3.4 BET analysis

The BET analysis was carried out to measure surface area and pore structures of as-prepared samples by nitrogen adsorption-desorption at 77 K. Results were depicted in Fig.7 for samples S0-S4. The adsorption-desorption isotherms of all samples can be assigned to type IV isotherm with an H3 type hysteresis loop, indicating the presence of mesopores (2-50nm in size) [27, 28]. The hysteresis loops of all the samples shift approach $p/p_0 = 1$, which suggests the presence of macropores (> 50 nm) [29]. The existence of Ag in Sb_2WO_6 has an obvious effect on the pore structure as shown in Table. 1. With the increase of Ag loading, the BET surface area of S1, S2 and S3 become larger than S0. Moreover, the pore volume of S2 and S3 is bigger than S0 and S1 and the pore average diameter of samples is larger than that of pure Sb_2WO_6 .

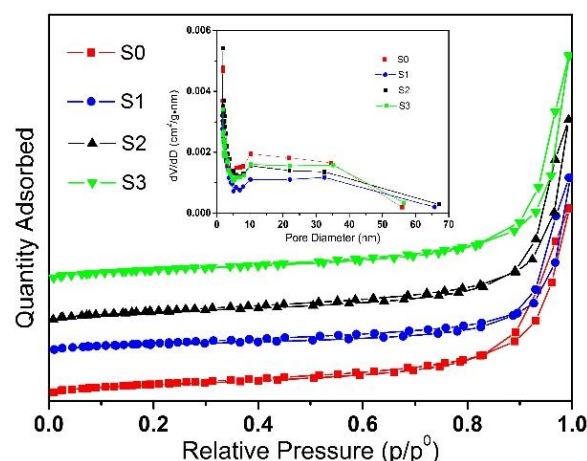


Fig. 7

Table.1

Sample	BET surface area (m ² /g)	Pore volume (cm ³ /g)	Average pore diameter (nm)
S0	30.4675	0.153090	18.97488
S1	31.2162	0.141663	25.61111
S2	31.8964	0.165286	21.17715
S3	32.5485	0.183404	23.36926

3.4. Photocatalytic activities

The Methyl orange (MO), Rhodamine B (RhB) were selected as model organic pollutants to evaluate photocatalytic activities of the as-prepared samples under different radiation sources. The UV light irradiation has a maximum wavelength of 362 nm, and the visible light source was employed too. The degradation curves of MO under UV light were shown in Fig. 8 for Sb₂WO₆ samples with different Ag weight loads. During a 30 min balance process of adsorption/desorption, the concentration of MO in solution decreased in the presence of the samples in the dark. The removal efficiencies are 5%, 25% and 10% for as-prepared samples S1, S2, S3, respectively. Fig. 8a, b and c present the UV-Vis absorption spectra of MO solution

with different samples. The characteristic absorption peak at $\lambda=462$ nm of MO is continuously redshifted with the UV irradiation time. This denotes a chemical catalytic degradation rather than a physical adsorption during the MO removal process. After 150 min UV light irradiation, the photocatalysis systems showed distinct degradation rate for MO. Compared with other samples, the S2 exhibited the highest degradation efficiency, with a final decomposition rate up to 92% as shown in Fig. 8d. The enhanced adsorption ability and photoactivity are probably due to the synergy effect between Ag atoms and Sb_2WO_6 . The strong adsorption ability can absorb MO molecules on the surface of Ag and Sb_2WO_6 , promoting the efficient contact of contaminated substrate and photo-induced holes. Consequently photocatalytic efficiency is enhanced. Interestingly, the S3 and S1 exhibited lower degradation efficiency than S2, indicating that the content of doped Ag could influence the photocatalytic activity in the removal of MO. During the photocatalytic process, it can't capture enough charges to separate photo-produced carriers effectively when Ag content $<20\%$. As more Ag was loaded, the photo-generated charges and holes would recombine easily to lower the photoactivity. Hence, the 20% is the suitable content for the composite. At this percentage, the migration efficiency of photo-induced electron is optimized, and inhibits the recombination of charges and holes effectively. As a result, the suitable ion doping has significant influence on photocatalytic activity of materials [30, 31].

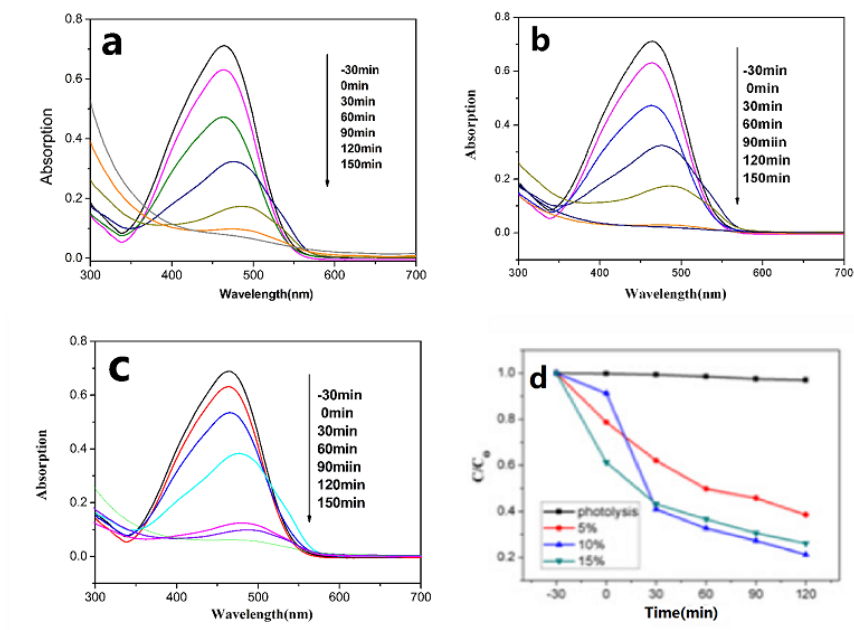


Fig. 8

Fig. 9a, b, c show the UV-vis adsorption spectra of RhB solution over different samples under UV light irradiation. The RhB characteristic absorption peak at $\lambda = 552$ nm gradually blue shifted with the increase of irradiation time. This is attributed to the fact that RhB was changed to some small molecule and then the conjugated structure was degraded under UV light irradiation. After 120 min of UV light irradiation, the absorption peak with the S2 disappeared, showing that almost all RhB pollutant was degraded, up to 98%. In contrast, the S1 and S3 sample didn't completely remove RhB. The degradation efficiencies are 64%, 89%, respectively (Fig. 9d). Hence, the S2 showed the highest photocatalytic ability. On the other hand, it can be seen that all the samples exhibited different degree adsorption on RhB, which were similar to those in MO solution. Moreover, the difference is that the degradation time of MO is longer than that of RhB. The results revealed that the Ag-loaded Sb_2WO_6 has a certain

selectivity in degradation of pollutants.

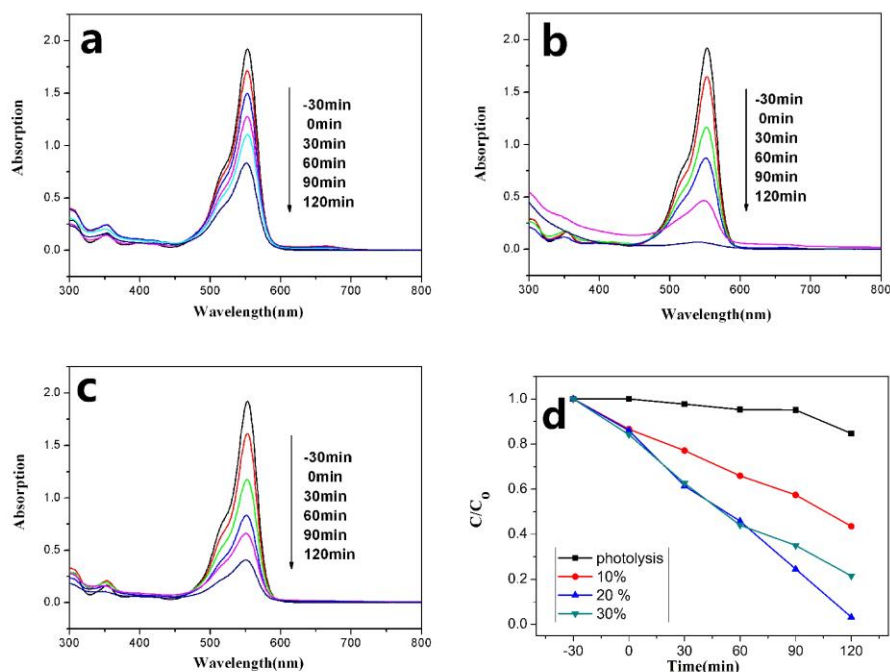


Fig. 9

The photocatalytic experiments were then carried out under visible light. The Methylene blue (MB) and Rhodamine B (RhB) were chosen as model pollutants. As shown in Fig. 10a, degradation rates of MB are 58.2%, 95.9%, 94.2% and 86.5% for S0, S1, S2, and S3, respectively. For comparison purpose, the MB without photocatalysts was also carried out. Only ~10% of MB was removed under visible light. In order to accelerate the photocatalytic degradation process, 3 drops of 30% H_2O_2 were added into MB solution. As shown in Fig. 10b, degradation rates for MB solution reached 99.2%, 99.3%, 99.5%, 99.4% and 34% for S0, S1, S2, S3 and the blank, respectively. With regard to S1, S2 and S3, the blue colour from the MB dispersion solution with H_2O_2 became colourless with 60 min visible light irradiation.

From the Fig. 10c, it can be seen that only 84.6%, 96.7%, 95.7%, 91.8% and 26.1% of RhB in RhB solution were removed for S0, S1, S2, S3 and blank, respectively. The degradation efficiencies of the samples for RhB were lower than that for MB at the same condition compared to Fig. 10b. This can be attributed to the complicated molecule structure of RhB. In all, the Ag doped Sb_2WO_6 samples show enhanced and excellent photoactivity compared to pure Sb_2WO_6 both under UV light and visible light irradiations.

The stability and reusability of photocatalysts are significant factors to meet economic and ecological demands in terms of “green chemistry”. The as-prepared samples also possess stability and reusability in visible light driven degradation process for MB. As shown in Fig. 10d, the efficiency over S2 with existence of H_2O_2 for MB is up to 94.9% after four cycles of degradation process. The results show that as-prepared samples can be reused.

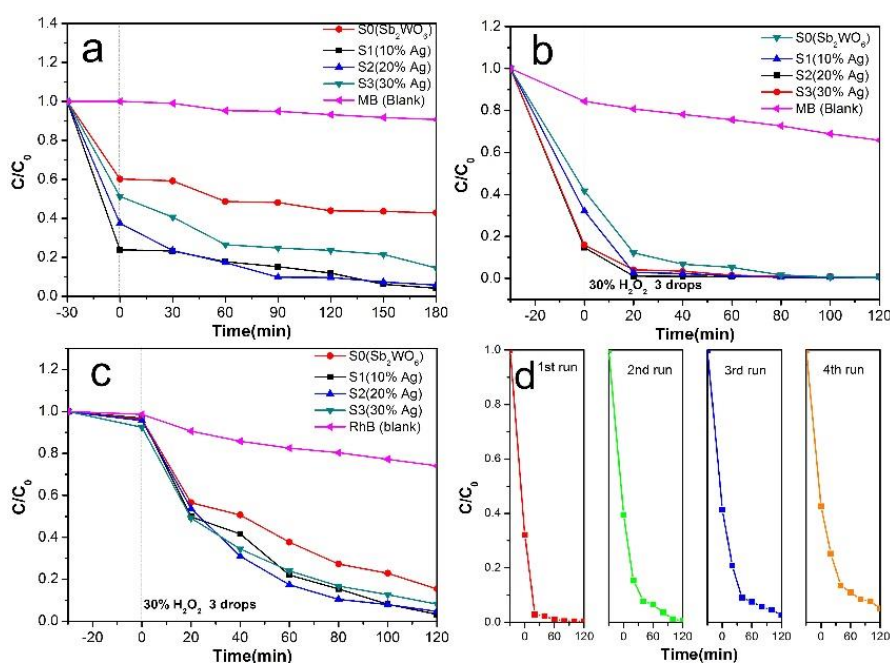


Fig. 10

Fig. 11 shows the comparative test between S2 and S0 for the degradation of MO, RhB after 90 min of UV light irradiation and MB, RhB after 80 min (or 90 min for MB without H₂O₂) visible light irradiation with 3 drops of 30% H₂O₂. After 90 min of UV light irradiation, the removal rate of S2 and pure Sb₂WO₆ are 82% and 35% for MO, and 87%, 38% for RhB. Moreover, with the visible light irradiation for 80 min, the removal rate of MB and RhB with 3 drops of 30% H₂O₂ is up to 92, 73% for S0, 99, 90% for S2, respectively. The S2 possessed highest photocatalytic ability among the Sb₂WO₆ samples both in degradations of MO and of RhB. Results demonstrate that metallic Ag doped in Sb₂WO₆ eventually enhanced the photocatalytic ability.

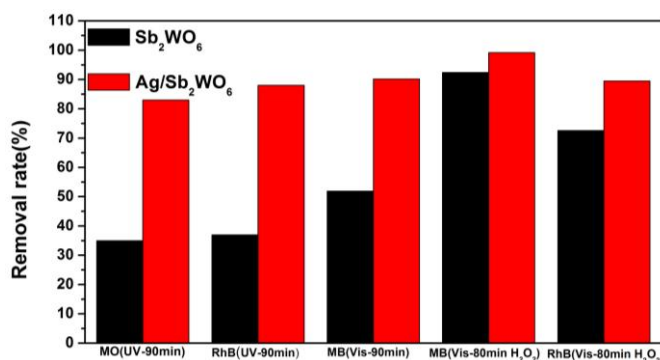


Fig. 11

In order to confirm the photodegradation degree of MB solution, the final solution samples which were treated by the photocatalysts S0, S1, S2 and S3 under visible light irradiation (3 drop 30% H₂O₂ added) were tested by TOC analysis. Table. 2 shows that the amount of residual total organic carbon is 10.9%, 8.89%, 10.4% and 10.3% for S0, S1, S2, S3, respectively. It indicates that the samples have excellent photoactivity under visible light and can oxidize MB pollutant to H₂O and CO₂.

Table.2

Sample	S0	S1	S2	S3
TOC(C/C ₀)(%)	10.9	8.89	10.4	10.3
TC(C/C ₀)(%)	11.6	9.59	13.1	11.1

3.4. Photocatalytic mechanism

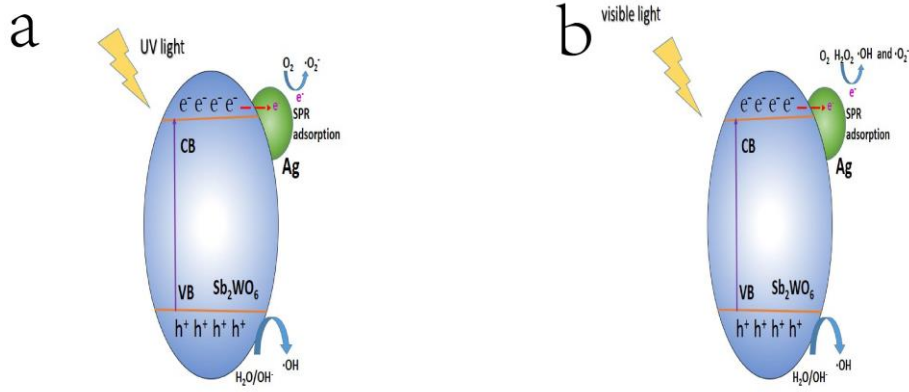


Fig. 12

For the degradation of RhB, MO and MB, a possible photocatalytic mechanism of photoelectron–hole pairs separation and transfer was proposed. In previous studies, the high photocatalytic activity under light irradiation is attributed to the synergy effect of many factors, such as generation efficiency and separation efficiency of photoelectron–hole pairs, hierarchical structure, surface areas and band gap of material itself. Here, the metallic Ag nanoparticles were loaded on the hierarchical material, benefiting the photocatalytic degradation of RhB and MO. The SPR (Surface Plasmon Resonance) effect which is induced by the light irradiation can produce strong local electronic field to enhance the energy of trapped electrons [32-37]. As shown in Fig. 12a, the photo-induced electrons can migrate from Sb_2WO_6 through a Schottky barrier to metallic Ag, which could lower the recombination rate of

photoelectron–hole pairs [38, 39,40 Shi et al., Small, 14:1704526 (2018)]. With the UV light irradiation, the electrons in valence band of Sb_2WO_6 was excited to the conduction band and migrate to Ag. The excited state of photo-induced electrons and holes can react with charge acceptor or donor to produce radicals such as $\bullet\text{O}_2^-$ and $\bullet\text{OH}$. Moreover the strong adsorption ability of the samples can absorb MO, MB and RhB molecules on the surface of Sb_2WO_6 or Ag nanoparticles. The absorbed species can be directly oxidized by these active radicals and turn to final products as H_2O and CO_2 . The microsphere with a great many number of nanosheets can improve the utilization efficiency of UV light by reflecting light multiply [40, 41]. For these reasons, the catalysts exhibited higher photocatalytic efficiency than the pure Sb_2WO_6 . As shown in Fig. 12b, under the visible light irradiation, electrons are transferred from the conduction band of Sb_2WO_6 to Ag. The excited state of photo-induced electrons can react with H_2O_2 and O_2 to produce radicals $\bullet\text{OH}$ and $\bullet\text{O}_2^-$, which increase photocatalytic efficiency.

In order to further confirm the above proposed photocatalytic mechanism for the Ag- Sb_2WO_6 system, experiments with certain scavengers and without any scavengers-loaded conditions were conducted. The isopropanol (IPA, 1mmol), benzoquinone (BQ, 1mmol) and disodium ethylenediaminetetraacetate (EDTA-2Na, 1mmol) were used for the $\bullet\text{OH}$, $\bullet\text{O}_2^-$ and hole (h^+) scavengers, respectively. The experiment has been performed to investigate the photocatalytic degradation process of RhB under ultraviolet light irradiation by S2 sample. As observed from Fig. 13, the photocatalytic degradation of RhB was substantially suppressed after IPA was added,

which indicates the $\bullet\text{OH}$ plays an important role in the degradation reaction. It can obviously observe that the addition of BQ also inhibited the degradation of RhB, suggesting that $\bullet\text{O}_2^-$ also is the main active specie of $\text{Ag-Sb}_2\text{WO}_6$ for degradation of RhB. However, ambiguous inhibition in the photocatalytic degradation efficiency was observed when EDTA-2Na was applied as h^+ scavenger. The free radicals trapping experiments indicate that the $\bullet\text{OH}$ and $\bullet\text{O}_2^-$ are the main active species to oxidize the dye solution, while h^+ plays a relatively minor role for dye degradation.

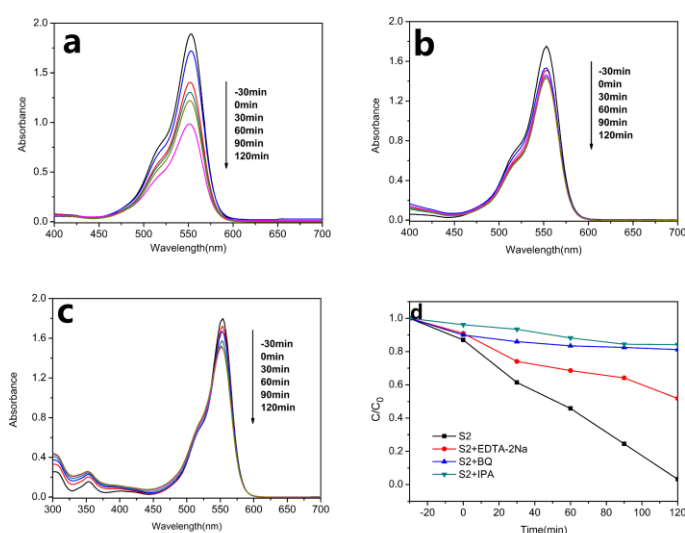


Fig. 13

4. Conclusions

In summary, the Ag-loaded Sb_2WO_6 photocatalysts with well-defined microsphere morphology have been successfully synthesized by a facile solvothermal method. Sodium tungstate, antimony trichloride and silver nitrate were used as W, Sb and Ag sources, respectively. Results show that the metallic Ag was doped in Sb_2WO_6 successfully and samples have larger BET surface area with a relatively narrow band

gap compared to the pure Sb_2WO_6 . The photocatalytic results exhibit that the photocatalytic activity of $\text{Ag-Sb}_2\text{WO}_6$ is excellent and superior to that of pure Sb_2WO_6 . The high photocatalytic ability of the Ag loaded system originates from SPR effect between Ag and Sb_2WO_6 , synergy effect of low recombination rate of photoelectron–hole pairs, and strong adsorption ability for pollutant.

Acknowledgements

The authors acknowledge with thanks the financial support of Scientific Research Fund of Hunan Provincial Education Department, China (16B253), the Open Project Program of State Key Laboratory of Structural Chemistry, China (No. 20150018) and Hunan 2011 Collaborative Innovation Center of Chemical Engineering & Technology with Environmental Benignity and Effective Resource Utilization and the profile grant of the Academy of Finland. T. Li acknowledges Oulu University Short-term International Research Visit grant during his stay in Finland. Authors thank A. A. Ovchinnikova for language improvement.

References

- [1] A. Kubacka, M. F. García, G. Colón, Advanced Nanoarchitectures for Solar Photocatalytic Applications. *Chem. Rev.* 2011, 112, 1555–1614.
- [2] W. H. Zhou, M. H. Cao, N. Li, S. Y. Su, X. Y. Zhao, J. Q. Wang, X. H. Li, C. W. Hu, Ag@AgHPW as a plasmonic catalyst for visible-light photocatalytic degradation of environmentally harmful organic pollutants. *MRS. Bulletin.* 2013, 48, 2308–2316.

- [3] S. G. D. Moraes, R. S. Freire, N. Durán, Degradation and toxicity reduction of textile effluent by combined photocatalytic and ozonation processes. *Chemosphere*. 2000, 40, 369–373.
- [4] X. Cao, Y. Oda, F. Shiraishi, Photocatalytic and adsorptive treatment of 2,4-dinitrophenol using a TiO₂ film covering activated carbon surface. *Chem. Eng. J.* 2010, 156, 98–105.
- [5] F. Li, Y. Dai, M. Gong, T. Yu, X. Chen, Synthesis, characterization of magnetic-sepiolite supported with TiO₂, and the photocatalytic performance over Cr(VI) and 2,4-dichlorophenol co-existed wastewater. *J. Alloys Compd.* 2015, 638, 435–442.
- [6] A. B. Murphy, P. R. F. Barnes, L. K. Randeniya, I. C. Plumb, I. E. Grey, M. D. Horne, J. A. Glasscock Efficiency of solar water splitting using semiconductor electrodes. *J. Hydrogen Energy*. 2006, 31, 1999–2017.
- [7] A. Fujishima, K. Honda, Electrochemical Photolysis of Water at a Semiconductor Electrode. *Nature*. 1972, 238, 37–38.
- [8] H. M. Yuan, J. L. Liu, J. Li, Y. P. Li, X. P. Wang, Y. Q. Zhang, J. B. Jiang, S. Y. Chen, C. Zhao, D. Qian. Designed synthesis of a novel BiVO₄–Cu₂O–TiO₂ as an efficient visible-light-responding photocatalyst. *J. Colloid Interf. Sci.* 2015, 444, 58–66.
- [9] H. B. Feng, Y. P. Li, D. M. Luo, G. R. Tan, J. B. Jiang, H. M. Yuan, S. J. Peng, D. Qian. Novel visible-light-responding InVO₄-Cu₂O-TiO₂ ternary

- nanoheterostructure: Preparation and photocatalytic characteristics. *Chin. J. Catal.* 2016, 37, 855–862.
- [10] S. Sakthivel, H. Kisch, Daylight Photocatalysis by Carbon-Modified Titanium Dioxide. *Angew.Chem. Int. Ed.* 2003, 42, 4908–4910.
- [11] C. Zhang, Y. Zhu, Synthesis of Square Bi_2WO_6 Nanoplates as High-Activity Visible-Light-Driven Photocatalysts. *Chem. Mater.* 2005, 17, 3537–3545.
- [12] S. Zhang, C. Zhang, Y. Man, Y. Zhu, Visible-light-driven photocatalyst of Bi_2WO_6 nanoparticles prepared via amorphous complex precursor and photocatalytic properties. *J. Solid State Chem.* 2006, 179, 62–69.
- [13] H. W. Newkirk, P. Quadflieg, J. Liebertz, A. Kockel, Growth, crystallography and dielectric properties of Bi_2WO_6 . *Ferroelectrics*, 1972, 4, 51–55.
- [14] V. I. Utkin, Yu. E. Roginskaya, V. I. Voronka, V. K. Yanovskii, B. S. Galyamov, Yu. N. Venetsev, Dielectric properties, electrical conductivity, and relaxation phenomena in ferroelectric Bi_2WO_6 . *Phys. Status Solidi*. 1980, 59, 75–82.
- [15] V. I. Utkin, Yu. E. Roginskaya, V. I. Voronkova, V. K. Yanovskii, B. Sh. Galyamov, Yu. N. Venetsev, Dielectric properties, electrical conductivity, and relaxation phenomena in ferroelectric Bi_2WO_6 . *Phys. Status Solidi A*. 1980, 59, 75.
- [16] S. Hu, C. Xu, F. Ma, L. Cao and L. Zhen, Solvothermal synthesis of orthorhombic Sb_2WO_6 hierarchical structures and their visible-light-driven photocatalytic activity. *Dalton Trans.* 2014, 43, 8439–8445.

- [17] J. Bi, Y. Liu, S. Liang, W. Wu, R. Yuan, Novel hierarchical architectures of Sb_2WO_6 : template-free hydrothermal synthesis and photocatalytic reduction property for azo compound. *J. Nanopart. Res.* 2013, 15, 1–10.
- [18] A. Martínez-de la Cruz and F. E. Longoria Rodríguez, Electrochemical lithium insertion in the solid solution $\text{Bi}_2\text{WO}_6\text{-Sb}_2\text{WO}_6$ with Aurivillius framework. *Mater. Res. Bull.* 2007, 42, 1851–1855.
- [19] K. Awazu, M. Fujimaki, C. Rockstuhl, J. Tominaga, H. Murakami, Y. Ohki, N. Yoshida and T. Watanabe, A Plasmonic Photocatalyst Consisting of Silver Nanoparticles Embedded in Titanium Dioxide. *J. Am. Chem. Soc.* 2008, 130, 1676–1680.
- [20] A. P. Zhang, J. Z. Zhang, Characterization and photocatalytic properties of Au/BiVO_4 composites. *J. Alloy. Compd.* 2010, 491, 631–635.
- [21] L. Ge, J. Mol. Novel visible-light-driven Pt/BiVO_4 photocatalyst for efficient degradation of methyl orange. *Appl. Catal. A- Chem.* 2008, 282, 62–66.
- [22] C. Y. Yang, F. Li, T. H. Li. A one-step ionic liquid-assisted ultrasonic method for the preparation of BiOCl/m-BiVO_4 heterojunctions with enhanced visible light photocatalytic activity. *CrystEngComm.* 2015, 17, 7676–7683.
- [23] Wang. J, Feng. D, Wu. W, Zeng. M, Li. Y. An investigation of the flame retardation mechanism of polypropylene containing a chlorine flame retardant system by XPS (ESCA). *Polym. Degrad. Stabil.* 1991, 31, 129–140.
- [24] E. V. Benvenutti, Y. Gushikem, A. Vasquez, S. C. D. Castro, G. A. P. Zaldivar. X-Ray photoelectron spectroscopy and mössbauer spectroscopy study of iron

- (III) and antimony (V) oxides grafted onto a silica gel surface. *J. Chem. Soc. Chem. Commun.*, 1991, 1325–1327.
- [25] J. He, W. Wang, F. Long, Z. Zou, Z. Fu and Z. Xu. Hydrothermal synthesis of hierarchical rose-like Bi_2WO_6 microspheres with high photocatalytic activities under visible-light irradiation. *Mater. Sci. Eng. B*, 2012, 177, 967–974.
- [26] Y. H. B. Liao, J. Wang, J. Lin, W. Chung, W. Y. Lin, C. Chen. Synthesis, photocatalytic activities and degradation mechanism of Bi_2WO_6 toward crystal violet dye. *Catalysis Today*, 2011, 174, 148–159.
- [27] F. Li, Y. Jiang, M. Xia, M. Sun, B. Xue, X. Ren, A high-stability silica–clay composite: Synthesis, characterization and combination with TiO_2 as a novel photocatalyst for Azo dye. *J. Hazard. Mater.* 2009, 165, 1219–1223.
- [28] J. L. Valentín, M. A. López-Manchado, A. Rodríguez, P. Posadas, L. Ibarra, Novel anhydrous unfolded structure by heating of acid pre-treated sepiolite. *Appl. Clay. Sci.* 2007, 36, 245–255.
- [29] T. B. Li, G. Chen, C. Zhou, Z. Y. Shen, R. C. Jin and J. X. Sun, New photocatalyst BiOCl/BiOI composites with highly enhanced visible light photocatalytic performances. *Dalton Trans.* 2011, 40, 6751–6758.
- [30] O. Bechambi, M. Chalbi, W. Najjar, S. Sayadi, Photocatalytic activity of ZnO doped with Ag on the degradation of endocrine disrupting under UV irradiation and the investigation of its antibacterial activity. *Appl. Surf. Sci.* 2015, 347, 414–420.

- [31] Y. Xue, X. Wang, The effects of Ag doping on crystalline structure and photocatalytic properties of BiVO₄. *Int. J. Hydrogen. Energ.* 2015, 40, 5878–5888.
- [32] J. X. Low, J. G. Yu, Q. Li and B. Cheng, Enhanced visible-light photocatalytic activity of plasmonic Ag and graphene co-modified Bi₂WO₆ nanosheets. *Phys. Chem. Chem. Phys.* 2014, 16, 1111–1120.
- [33] S. C. Warren, E. Thimsen, Plasmonic solar water splitting. *Energy Environ. Sci.* 2012, 5, 5133–5146.
- [34] J. G. Yu, G. P. Dai and B. B. Huang, Fabrication and Characterization of Visible-Light-Driven Plasmonic Photocatalyst Ag/AgCl/TiO₂ Nanotube Arrays. *J. Phys. Chem. C.* 2009, 113, 16394–16401.
- [35] J. Ren, W. Z. Wang, S. M. Sun, L. Zhang, J. Chang, Enhanced photocatalytic activity of Bi₂WO₆ loaded with Ag nanoparticles under visible light irradiation. *Appl. Catal. B. Environ.* 2009, 92, 50–55.
- [36] K. Awazu, M. Fujimaki, C. Rockstuhl, J. Tominaga, H. Murakami, Y. Ohki, N. Yoshida and T. Watanabe, A Plasmonic Photocatalyst Consisting of Silver Nanoparticles Embedded in Titanium Dioxide. *J. Am. Chem. Soc.* 2008, 130, 1676–1680.
- [37] X. Fan, J. Fan, X. Hu, E. Liu, L. Kang, C. Tang, Y. Ma, H. Wu, Y. Li, Preparation and characterization of Ag deposited and Fe doped TiO₂ nanotube arrays for photocatalytic hydrogen production by water splitting. *Ceram. Int.* 2014, 40, 15907–15917.

- [38] F. Dong, P. D. Li, J. B. Zhong, X.Y. Liu, Y. X. Zhang, W. L. Cen and H. W. Huang, Simultaneous Pd^{2+} doping and Pd metal deposition on $(\text{BiO})_2\text{CO}_3$ microspheres for enhanced and stable visible light photocatalysis. *Appl. Catal. A-Gen.* 2016, 510, 161–170.
- [39] R. Su, R. Tiruvalam, A. J. Logsdail, Q. He, C. A. Downing, M. T. Jensen, N. Dimitratos, L. Kesavan, P. P. Wells, R. Bechstein, Designer Titania-Supported Au–Pd Nanoparticles for Efficient Photocatalytic Hydrogen Production. *ACS Nano.* 2014, 8, 3490–3497.
- [40] N. Kılınç, E. Şennik, M. Işıka, A.Ş. Ahsena, O. Öztürka, Z.Z.Öztürka, Fabrication and gas sensing properties of C-doped and un-doped TiO_2 nanotubes. *Ceram. Int.* 2014, 40, 109–115.
- [41] C. Y. Yang, X. J. Yang, F. Li, T. H. Li, W. Cao, Controlled synthesis of hierarchical flower-like Sb_2WO_6 microspheres: Photocatalytic and superhydrophobic property. *J. Ind. Eng. Chem.* J. Ind. Eng. Chem. 2016, 39, 93–100.

Figure and table captions

Fig. 1. XRD patterns of S0; S1; S2; S3 samples.

Fig. 2. SEM images of S0 (a); S1 (b); S2 (c); S3 (d).

Fig. 3. TEM (a, b) and HRTEM (c, d) images of S2 composite.

Fig. 4. Nanostructure of S2. (a-b) HAADF-STEM image, and (c–h) the corresponding EDS elemental mapping images, (g) a typical EDS spectrum.

Fig. 5. XPS spectra of S2 (a)Sb 3d; (b) W 4f; (c) O 1s; (d)C 1s; (e) Ag 3d; and (f) survey.

Fig. 6. UV-Vis diffuse reflectance spectrum of S0; S1; S2 and S3.

Fig. 7. Nitrogen adsorption-desorption isotherms for the S0; S1; S2 and S3. Inset: the corresponding pore-size distribution of S0; S1; S2 and S3.

Fig. 8. UV-Vis absorption spectra of MO solution after being treated with as-prepared samples S1 (a); S2 (b); S3 (c) and (d) Time-course variation of C/C_0 of MO solution under UV light irradiation in the presence of the as-prepared samples.

Fig. 9. UV-Vis absorption spectra of RhB solution after being treated with as-prepared samples S1 (a); S2 (b); S3(c) and (d) Time-course variation of C/C_0 of RhB solution under UV light irradiation in the presence of the as-prepared samples.

Fig. 10. (a) Time-course variation of C/C_0 of MB solution under visible light over the samples of S0, S1, S2 and S3; (b) Time-course variation of C/C_0 of MB solution with H_2O_2 under visible light over the samples of S0, S1, S2 and

S3; (c) Time-course variation of C/C_0 of RhB solution with H_2O_2 under visible light over the samples of S0, S1, S2 and S3. (d) Cycle experiments of MB degradation over S2.

Fig. 11. Comparative test between S2 (Ag/Sb_2WO_6) and S0 (pure Sb_2WO_6) for degradation of MO, RhB after 90 min of UV light irradiation and MB, RhB after 80 min (or 90 min for MB without H_2O_2) of visible light irradiation with 3 drops of 30% H_2O_2 .

Fig. 12. Schematic illustration of the photocatalytic mechanism of Ag/Sb_2WO_6 microspheres under a (a) UV light irradiation (b) visible light irradiation.

Fig. 13. UV-Vis absorption spectra of RhB solution over the obtained S2 in the presence of different scavengers: (a) EDTA-2Na; (b) BQ; (c) IPA. (d) Time-course of the photodegradation of RhB with S2 as the photocatalyst in the presence of various scavengers.

Table. 1. BET surface area, pore volume and average pore size of the samples.

Table. 2. The C/C_0 of final TOC and TC in MB solution under visible light over the samples of S0, S1, S2 and S3